Wind-Energy Generation by Active Flow Control

David Greenblatt, Gilad Doron and Alexander Treizer
Technion – Israel Institute of Technology, Technion City, Haifa 32000, Israel

Received date: 1/1/2014; Accepted date: 7/7/2014

ABSTRACT
This paper presents and tests a novel wind-energy generator that is driven by active flow control. To achieve this, flow-control-induced oscillations were forced by dynamic boundary layer separation and attachment using plasma actuators. Proof-of-concept wind tunnel experiments, at a subcritical Reynolds number of 80,000, were performed on a one-degree-of-freedom pivoted cylindrical body where pulsed dielectric barrier discharge plasma actuators were used to control separation. A nonlinear load, typical of a positive displacement fluid pump, was attached to the system and calibrated. Using phase-locked actuation, simultaneous pressure and angular displacement measurements were performed to determine the integrated mean system power. A system model, including non-linear load effects, aerodynamic effects and friction was developed. Peak measured power coefficients were relatively small, less than 1%; nevertheless the power required to drive the actuators was one order of magnitude lower than the measured system power. The system model was solved using a fourth-order Runge-Kutta method and the integrated power predictions were excellent. Friction was found to play a significant role in reducing the power output of the generator. Despite these modest results, the system may be amenable to up-scaling because lateral force coefficients can be increased and the power coefficient increases with the square-root of the system dimensions.

1. INTRODUCTION

Horizontal axis wind turbines (HAWTs) are a major source of renewable energy with worldwide total installed capacity growing exponentially [1]. As designers attempt to increase the physical size of the turbines to reduce the cost of energy, mechanical loads – and in particular fatigue loads – become increasingly difficult to manage [2]. Moreover, with the present trend towards deep-water offshore wind energy, the HAWT paradigm with a heavy nacelle and blades poses significant stability problems.

The purpose of this paper is to present a new paradigm for wind energy generation that is based on active flow control; in particular, active boundary layer separation control is exploited to generate reciprocating motion which can be harnessed as energy. For example, reciprocating motion can be converted to rotary motion or used directly for energy generation via linear generators, or for drilling, pumping or compressing air as a means of energy storage. The concept described here facilitates a simple design that eliminates rotating blades and brings the center of gravity close to the water or ground level. Possibly the first attempt to extract wind energy based on reciprocating motion was reported by Bade [3], who developed a wing with passive-pitch articulation, mounted on the end of a pivoted boom. Around the same time, Jeffery [4] developed a vertical swinging-wing that was pivoted and made to “flap” in the wind. McKinney and DeLauriert [5] considered a wing that oscillates simultaneously in both angle-of-attack and vertical translation, termed a “wingmill”. They conducted both an analytical and an experimental investigation, where phasing between the angle-of-attack and vertical translation was prescribed. An important result of their work was that the measured efficiencies were comparable to rotary designs.

The present investigation aims to take this concept a step further by using active separation control – or, in principle, any form of active flow control – instead of changing the wing or body angle-of-attack. This is realized here by exploiting dynamic attachment and separation of the boundary layer to produce reciprocating motion. It should also be evident that this means of energy generation is therefore fundamentally different from methods that exploit flow-induced or vortex induced vibrations [6]. This is because the forcing frequency is arbitrarily selected and, therefore, not related to the vortex shedding frequency in any way. In the present application, the forces produced by attaching and separating the flow periodically drive the body at, or near, resonance where the maximum power is produced. Greenblatt et al. [7] examined this concept on an unloaded one-degree-of-freedom pivoted cylindrical body using a single pulsed dielectric barrier discharge plasma actuator. The merits of using a cylindrical body are debatable, but the setup facilitated convenient separation control for a range of subcritical Reynolds numbers, corresponding to wind tunnel speeds between 4m/s and 10m/s. Periodic loading of the cylinder was achieved by periodic modulation of the actuator and large amplitude oscillations were observed when the modulation frequency was close to the system natural frequency.

This paper represents a natural follow-on study where we conduct experiments with two DBD plasma actuators at Re = 80,000. We develop a simple analytical model and a numerical model that includes both the damping due to a useful load as well as frictional losses (section 2). A proof-of-concept experiment, simulating a fluid pump, is then setup (section 3) where representative static load and flowfield data are presented (section 4). This is followed by the system calibration (section 5) after which the net power is measured (section 6) and the models are validated (section 7). Finally, aspects relating to up-scaling the generator to a kilo or megawatt utility-type machine are discussed (section 8) and followed by conclusions (section 9).

2. CONCEPT AND ANALYTICAL MODEL

2.1. System Modeling

Figure 1 shows the basic design of the Reciprocating-motion Wind-energy Generator (RWG). It consists of a large lightweight cylinder attached to a sting and mounted on a pivot that has a counterweight below. The center of gravity (CG) of the system is below the pivot to ensure stability. In general, the sting is mounted so that the device can oscillate on two axes: lateral (left-right motion; shown in the figure) and longitudinal (forward-backward motion, not shown). Active flow control devices are deployed on the cylinder so as to produce unsteady separation and attachment of the boundary layer. This results in large asymmetric aerodynamic loads that are used to drive the system in an oscillatory manner. A load, for example a linear generator (C_θ), can be attached to the pivot (as shown) or attached to the lower end of sting in the vicinity of the counter-weight. Similarly, gears

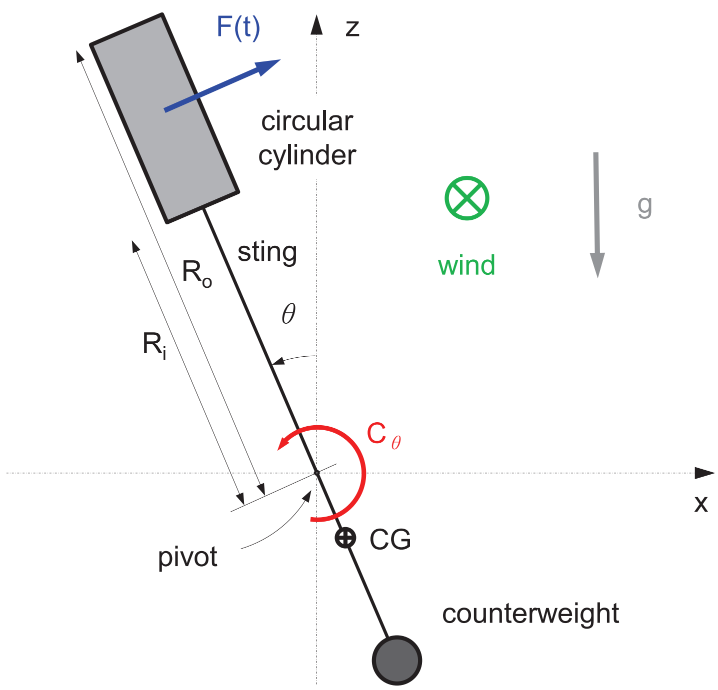

Figure 1. Basic concept of the 1-DOF RWG model considered in this study. The force $F(t)$ acts only in the x–z plane-of-motion; gravity acts in the $-z$ direction.

mounted on the shafts can be used to drive high-speed generators. The system can be designed to produce oscillatory forces in the lateral and longitudinal directions, in two degrees-of-freedom (2-DOF). Hence a total of four generators (two lateral; two longitudinal) can be employed.

For purposes of simplicity, we consider the RWG as an inverted pendulum that only oscillates in the plane perpendicular to the wind direction (1-DOF model) as depicted in the figure. It is forced by flow control devices on the cylinder and balanced by the mass below the 1-DOF pivot.

2.2. Analytic Linear Model

In this section we consider the idealized energy that can be extracted from the system. A simple model of the 1-DOF system (fig. 1) can be written as

$$J_0\ddot{\theta} + C_\theta\dot{\theta} + k_t \sin\theta = M(t) \tag{1}$$

where J_0 is overall moment of inertia with respect to the pivot, C_θ is the angular damping coefficient, k_t is the "dynamic stiffness", expressed as $m\ g\ l_{CG}$ and $M(t) = R{\cdot}F(t)$ is the driving moment. For simplicity, we assume a harmonic driving moment

$$M(t) = M_0 \cos \omega t \tag{2}$$

where $M_0 = R{\cdot}F_0$ and R is the distance from the pivot to the position of the resultant aerodynamic force, assumed to act at the center of the cylinder:

$$R = \tfrac{1}{2}(R_i + R_o) \tag{3}$$

where R_i and R_o as the distances from the pivot to the lower (inner) and upper (outer) edges of the cylinder respectively. This result is valid as long as we assume that $R\dot{\theta}_{\max} << U_\infty$. Combining equations 1 and 2 and assuming small angles, results in:

$$J_0\ddot{\theta} + C_\theta\dot{\theta} + k_t\theta = M_0 \cos\omega t \tag{4}$$

This equation has the well-known solution:

$$\theta(t) = \theta_0 \cdot \cos(\omega t - \phi) \tag{5}$$

The pendulum will oscillate at the same frequency of the applied torque but with a phase shift ϕ. The terms on the right hand side of equation 5 are:

$$\theta_0 = \frac{M_0}{\sqrt{(k_t - J_0\omega^2)^2 + (C_\theta\omega)^2}} \tag{6}$$

and

$$\phi = \tan^{-1}\left(\frac{C_\theta\omega}{k_t - J_0\omega^2}\right) \tag{7}$$

To obtain similarity equations, we define the dimensionless parameters:

$$\omega_n = \sqrt{\frac{k_t}{J_0}} \tag{8}$$

$$C_c = 2J_0\omega_n \tag{9}$$

$$\zeta = \frac{C_\theta}{C_c} \tag{10}$$

and

$$\frac{C_\theta}{J_0} = 2\zeta\omega_n \tag{11}$$

where ω_n is the system natural frequency, and ζ is the damping ratio. The deflection angle produced by the static moment M_0, (measured in radians) and the frequency ratio are defined, respectively, as:

$$\theta_{st} = \frac{M_0}{k_t} \tag{12}$$

$$r = \frac{\omega}{\omega_n} \tag{13}$$

After substituting we get:

$$\theta_0 = \frac{\theta_{st}}{\sqrt{(1-r^2)^2 + (2\zeta r)^2}} \tag{14}$$

$$\phi = \tan^{-1}\left(\frac{2\zeta r}{1-r^2}\right) \tag{15}$$

The average power produced over one cycle is obtained via the integration:

$$P = \frac{1}{T}\int_0^T M(t)\cdot\dot{\theta}\,dt = \frac{1}{2}M_0\cdot\theta_0\cdot\omega\cdot\sin\phi \tag{16}$$

Let us now assume aerodynamic force amplitude of:

$$F_0 \cong C_L\cdot q_\infty\cdot h\cdot d \tag{17}$$

where C_L is the maximum lateral aerodynamic force coefficient, and h is the cylinder span; this is valid as a result of the assumption $R\dot{\theta}_{\max} << U_\infty$. For wind turbines, the power coefficient is defined as:

$$C_P = \frac{P}{q_\infty U_\infty A_s} \tag{18}$$

where A_s is the swept area of the turbine.[1] For the present geometry, the swept area depends upon the cylinder dimensions as well as the peak oscillation amplitudes. Therefore, after substitution, the power coefficient can be written as

$$C_P = \frac{\frac{1}{2}M_0\theta_0\omega}{q_\infty U_\infty(2\theta_0 R + d)h}\sin\phi \tag{19}$$

or alternatively

$$C_P = \frac{C_L}{4}\frac{\omega_n d}{U_\infty}\frac{1}{1+d/(2R\theta_0)}\cdot r\cdot\sin\phi \tag{20}$$

As noted by Greenblatt et al. [7], the peak power coefficient expressed in equation 20 is only limited by the lateral force coefficient and reduced velocity $\omega_n d/U_\infty$, providing that the linear assumptions are not violated. It should be appreciated that the present analysis is fundamentally different to conservation laws applied to the flow through an idealized actuator disk. The latter analysis results in a maximum power coefficient, the so-called Betz limit, of 16/27. The present analysis also includes idealized limiting assumptions, in particular the small angle assumption and $R\dot{\theta}_{\max} << U_\infty$; therefore direct comparisons to the Betz limit should be avoided.

2.3. Energy Loss Mechanisms

The expression for C_P in equation 20 represents the ideal system power coefficient with zero aerodynamic or frictional losses. It assumes that the power imparted to the cylinder is delivered without loss to the load. In practice, losses must be accounted for and these can be considered as aerodynamic and frictional losses. A physically representative form of equation 1 can be written as:

$$J_0\dot{\theta} + \underbrace{c_l\dot{\theta} + c_d\dot{\theta} + M_f\,\mathrm{sgn}(\dot{\theta})}_{\text{total damping}} + k_t\sin\theta = M(t) \tag{21}$$

where c_l represents the useful load (damping coefficient), c_d is the damping coefficient due to aerodynamic drag (see [7]) and M_f is the torque loss due to friction in the damper or so-called Coulomb damping. Equation 21 can be solved numerically and then the useful power generated can be calculated according to:

$$P = \frac{1}{T}\int_0^T (c_l\dot{\theta})\dot{\theta}dt \tag{22}$$

where c_l can be non-dimensionalized as follows: $\zeta_l = c_l/2J_0\,\omega_n$.

[1] Note that the definition of swept area used here includes the dimensions of the cylinder and is therefore larger than that defined by [7].

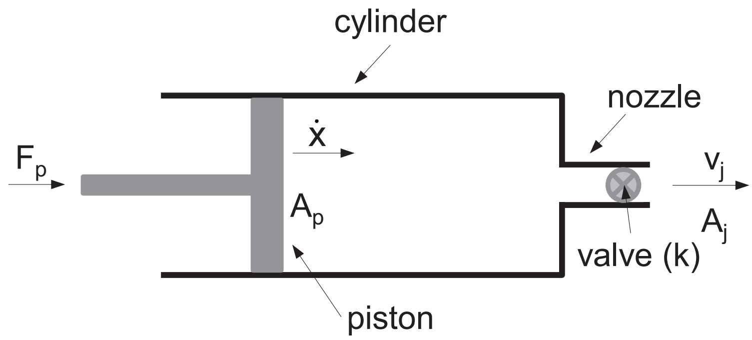

Figure 2. Schematic of the damper representing a non-linear “fluid pump” employed here.

2.4. Non-linear Load

In this study, a non-linear damper typical of a fluid pump was attached to the system at a variable distance l' from the pivot. The essential features of the fluid pump were a circular cylinder, piston and exit nozzle (see fig. 2). The application of a force F_p to the piston produced an air jet v_j. In practice, the load was variable by means of a valve at the nozzle exit, and this is described in section 3.

From simple conservation of mass, considering an incompressible flow:

$$v_j = \frac{A_p}{A_j}\dot{x} \tag{23}$$

Furthermore, applying Bernoulli’s equation on a streamline within the damper and rearranging:

$$p_p - p_{\text{atm}} = \frac{1}{2}\rho\left[\, v_j^2(1+k) - \dot{x}^2 \right] \tag{24}$$

where p_{atm} is the local atmospheric pressure and k is a variable nozzle pressure-loss coefficient. Letting $F_p = (p_p - p_{\text{atm}})A_p$, assuming that $\dot{x} = l'\dot{\theta}$ and combining equations 23 and 24 we can express the pump moment as:

$$M_p = l' c_q \dot{\theta}^2 \tag{25}$$

where

$$c_q = \frac{1}{2}\rho A_p l'^2 \left[\left(\frac{A_p}{A_j}\right)(1+k) - 1\right] \tag{26}$$

To account for the non-linear load in the form of quadratic damping attached to the system, equation 21 above is modified as follows:

$$J_0\ddot{\theta} + c_q\dot{\theta}^2 + c_d\dot{\theta} + M_f\,\text{sgn}(\dot{\theta}) + k_t\sin\theta = M\cos\omega t \tag{27}$$

Consideration of the frictional losses, expressed as M_f, will be considered in section 5.

3. EXPERIMENTAL SET-UP

Experiments were conducted in a low-speed wind tunnel with test section dimensions 100 cm × 61 cm × 200 cm (height, width and length). The maximum wind speed and turbulence level were 55m/s and 0.1% of U_∞, respectively. The model, shown in figs. 3a and 3b, consisted of a Plexiglas pendulum of mass 1.022 kg (d = 150 mm, h = 204 mm); a pivot-mounted rigid Plexiglas connecting rod and a damper mounted above the tunnel (see fig. 3a). The pivot rotated on a low-friction ball bearing, but could also be locked to prevent motion; this was used to facilitate flowfield measurements (see section 4). The angular position on the cylinder, measured from the vertical plane parallel to U_∞, was designated α (see [7] for more details). The cylinder was equipped with two surface-mounted DBD plasma actuators, mounted at $\alpha = \pm 80°$ that extended along the entire height h (see schematic in fig. 3b). Electrical cables used to drive the actuators were taped to the connecting rod and routed to a high voltage ac source above the wind tunnel (see below). The connecting rod was extended above the wind tunnel and connected to a load, in the form of a non-linear damper, characterized in section 2.4. A detailed description of the physical damper and associated pressure measurements made within its cylinder are described below.

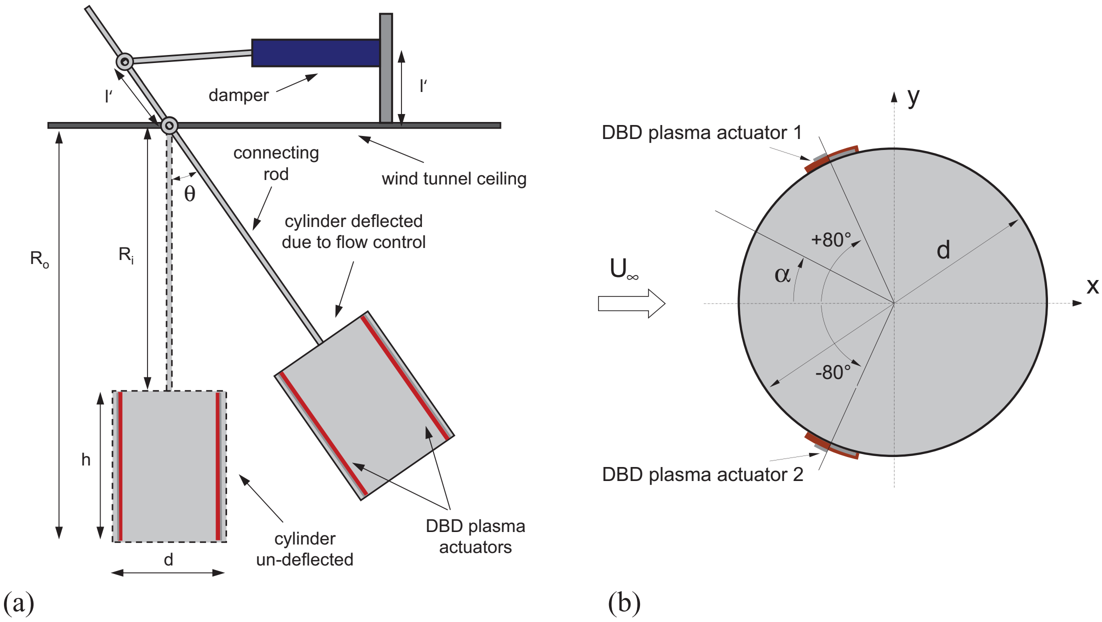

Figure 3. (a) Cylinder and connecting rod configuration viewed from upstream with relevant dimensions and definitions; (b) Underside view schematic of the cylinder showing the actuator locations (actuator thickness exaggerated for clarity).

Both DBD actuators used were based on the asymmetric wall-mounted configuration as described by Corke et al. [8]. The upper (exposed) and lower (encapsulated) electrodes (both 70 μm thick) were separated by three layers of 50 μm thick Kapton® tape, identical to that described in [7]. The high voltages were generated using two Minipuls-2 high voltage inverters (GBS Electronik); one for each actuator. The wave form was generated by means of an input signal and a low voltage (V_{in} < 30 V dc) source, while the dc current drawn by each actuator (I_{in}) was measured using Fluke 115C multimeters). This simplified the estimation of gross power (including all losses) dissipated in the actuators, namely $P_{in} = V_{in} I_{in}$. Ionization of the air, within the electric field, produced the pulsed body forces that were exploited here for controlling flow separation. Greenblatt et al. [7] conducted a detailed parametric study for a wide range of wind tunnel speeds, pulsation frequencies and plasma angles. On the basis of the parametric study, all present experiments were conducted at $U_\infty = 8$ m/s, while both actuators were driven at 8kV$_{pp}$ with f_{ion} = 10kHz and pulsations at f_p = 114Hz corresponding to $F^+ \equiv f_p d/U_\infty = 2.1$. It was ascertained in [7] that placement of the actuators at $\alpha = \pm 80°$ produced the largest lateral force coefficients. The duty cycle, defined as the percentage (or fraction) of the period that the actuator is operational, was varied in the range $0.1\% \leq DC \leq 50\%$. A typical ionization frequency, pulsed plasma frequency and duty cycle are shown in fig. 4a.

In a similar manner to [7], the location of the cylinder lower surface at any instant, and hence the determination of the deflection angle θ, was achieved optically. This involved filming the base of the cylinder, painted matt-black, using a Casio EX-F1 high-speed video camera with a resolution of 6 megapixels and a maximum of 1,200 frames per second (fps). A pattern recognition technique was used to determine the centroid within each frame. Several free-release experiments in still air were performed and these indicated a natural frequency f_n (virtually un-damped) of 0.790 Hz that compared favorably with the theoretical value of 0.794 Hz.

In Greenblatt [7], the pulsed plasma actuator was modulated at the excitation frequency f_{ex} in an open loop manner. In this investigation, two optical sensors (see fig. 5), one for each actuator were used to initiate the plasma signals in a phase-locked, or closed-loop, manner at $F^+ = 2.1$. An excitation period is illustrated in fig. 4b, where $f_{ex} < f_p$; in this example the $T_{act}/T_{ex} = 30\%$ per actuator. The actuation time (or time to termination) T_{act} was determined by specifying the number of plasma pulses.

The external load used for these experiments was an Airpot® model 2KS444 damper (see figs. 5 and 6) with characteristics typical of a positive displacement pump. It was constructed from a quartz glass cylinder with an internal low-friction sliding piston made from graphite. The outer part of the damper was covered with a rubber sheath to prevent damage. A circular cross-section rod was

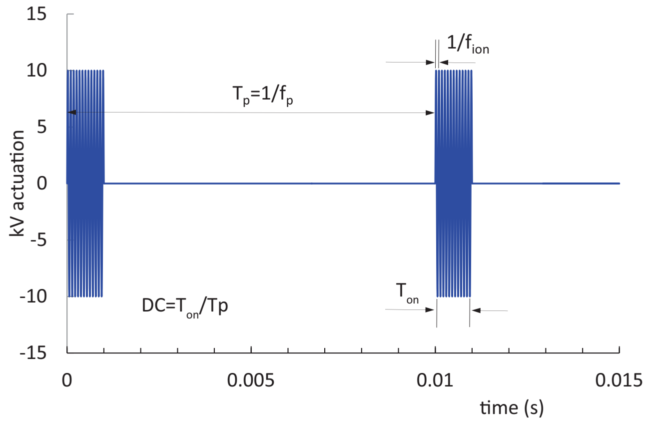

Figure 4. (a) Illustration of the pulsed plasma actuation where the plasma actuator is driven at 10 kHz and pulsed at 100 Hz with DC = 10% (from Greenblatt [7]).

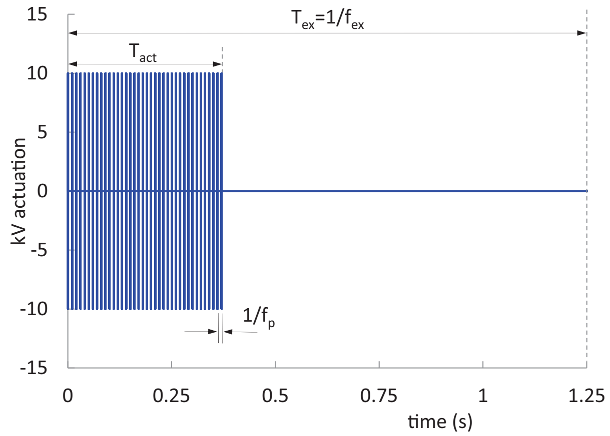

Figure 4. (b) Illustration of the pulsed plasma actuation of 100 Hz corresponding to Fig. 4(a) where the activation time T_{act} is 30% of the excitation period T_{ex} (adapted from Greenblatt [7]).

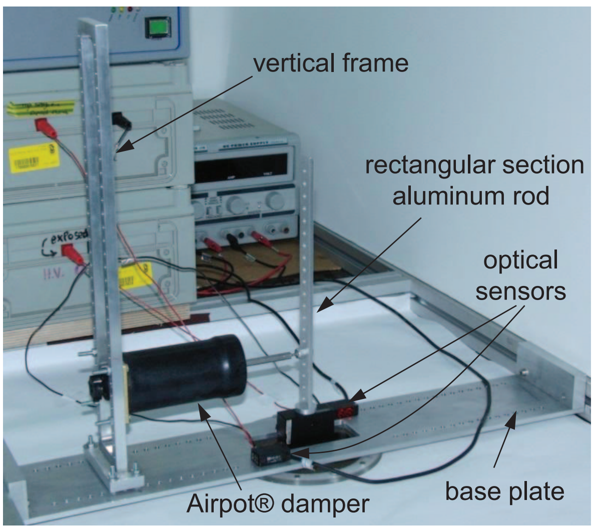

Figure 5. Photograph of the damper mounted on its frame and connected to the pendulum via a rod.

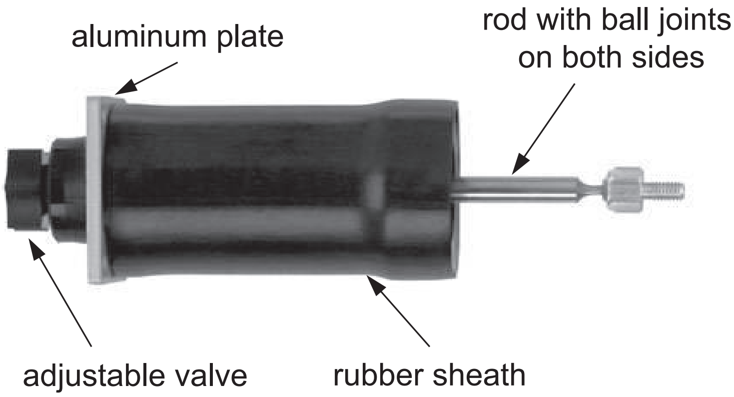

Figure 6. The Airpot® damper used in the present experiments.

connected to the piston, via a ball-joint. The free end of the rod was also equipped with a ball joint and threaded section (see fig. 6). The opposite end of the damper was equipped with an aluminum plate containing a nozzle and adjustable valve that allowed variation of the damping coefficient from a fully sealed state to a fully open state (see table 2 for the nominal damper specifications).

The damper was located in position by means of a vertical frame that was bolted to a horizontal base plate. The frame was composed of two vertical columns with 4 mm holes and 12 mm spacing between the holes to allow variation of its height. The base plate was bolted to the frame above the wind tunnel ceiling. A rectangular section aluminum rod with corresponding 4 mm holes and 12 mm spacing was mounted on the upper part of the system above the pendulum. The threaded part of the circular damper rod was inserted into the required hole of the rectangular section rod and fastened with a nut. With this setup, the degree of damping could be varied with a high degree of accuracy using the corresponding holes on the frame and rod. The base plate was also equipped with holes 10 mm apart to facilitate horizontal displacement of the damper.

Power measurement required the instantaneous measurements or estimation of the piston force $F_p(t)$ and its speed $\dot{x}(t)$. $F_p(t)$ was estimated by measuring the damper pressure $p_d(t)$ with the conventional assumption that $p_p(t) = p_d(t)$ with $F_p(t) = p_p(t)A_p$. The speed was $\dot{x}(t)$ estimated by numerically differentiating the instantaneous $\theta(t)$ data using central differences, combined with the system geometry. To measure the pressure, four symmetric pressure ports were installed in the rear aluminum plate. The ports were constructed from stainless steel tubes (1.6 mm OD and 0.8 mm ID) that were attached to the rear plate of the damper using epoxy adhesive (see fig. 7). The ports were connected to individual ports of a 10"WC Electronic Pressure Scanner (ESP modules) (Pressure Systems) using 30 mm lengths of vinyl tubing. The scanner is equipped with 32 pressure ports (4 were used

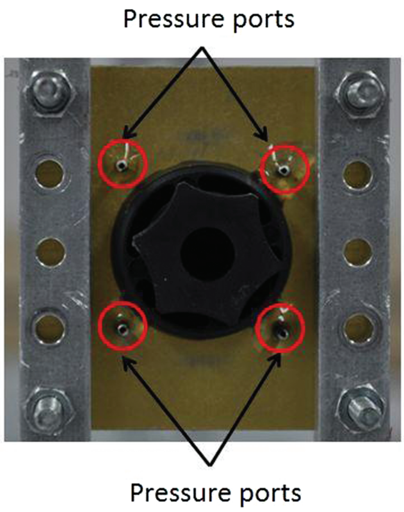

Figure 7. Photograph of the damper from the rear showing the four pressure ports.

corresponding to the 4 pressure ports) and measures differential pressure by means of an array of silicon piezoresistive pressure sensors, one for each pressure port. All differential pressure measurements were made relative to the ambient atmospheric conditions. Calibration and temperature compensation of the scanners was performed by a so-called Digital Temperature Compensation (DTC) Intium, which is a data acquisition system combined with digital temperature compensation to maintain optimal accuracy. The system was supplied with a manufacturer accuracy of ± 0.05%FS with a maximum of 600 Hz per Channel throughput capability.

4. STATIC LOADS & FLOWFIELD MEASUREMENTS

4.1. Mean Lateral Forces

Static lateral-force coefficients were determined as a function of the plasma control parameters at wind tunnel speeds U_∞ between 4 m/s and 10 m/s as described in Greenblatt et al. [7]. Briefly, experiments were performed without load by initiating the plasma and then recording the deflection angle after oscillations had decayed to negligible amplitude. This process was repeated for a wide variety of different parameters. The mean deflection angle relative to the un-deflected zero-angle was recorded and the lateral-force F_0 acting on the cylinder was calculated according to a simple static moment balance. The largest forces were recorded when the perturbations were introduced close to the separation angle (see fig. 8) which was measured, by means of tufts, to be between 70° and 80°. It has been shown previously that amplification of the perturbations is rooted in the shear layer instability [10]; here maximum lateral forces observed for the range $1 \le F^+ \le 2$ consistent with [11] and [12]. Important for a power balance, very little difference in lateral-force coefficient was measured for the range 0.1% to 50% duty cycle range [10].

4.2. Flowfield Measurements

Flowfield measurements were conducted using two-dimensional particle image velocimetry (PIV) where the pivot was locked at $\theta = 0°$; full details are provided in [7]. The absolute velocity $c = (u^2 + v^2)^{1/2}$ together with velocity vectors and the nondimensional vorticity ω_z are shown for the baseline case (figs. 9a and 9b) and the pulsed plasma corresponding to the $F^+ = 2.1$ case at $\alpha_f \approx 80°$ (figs. 10a and 10b). Based on these data, the baseline separation point was estimated to be $\alpha \approx 80°$, which was consistent with tuft-based flow visualization and comparable to the observations of Jukes and Choi, 2009. With plasma pulsations the separation location moved aft to $\alpha \approx 120°$ and similar results were observed at $F^+ = 1$ consistent with the similar lateral-force measurements (fig. 8) with minor changes to wake on the opposite side of the cylinder.

Following these experiments, phase-resolved PIV data were acquired during the attachment and separation transients, following the initiation and termination of pulsed pulsations, at $F^+ = 2.1$ (not shown, see [7]). Following initiation of the plasma pulsations, the separated shear layer attached to the

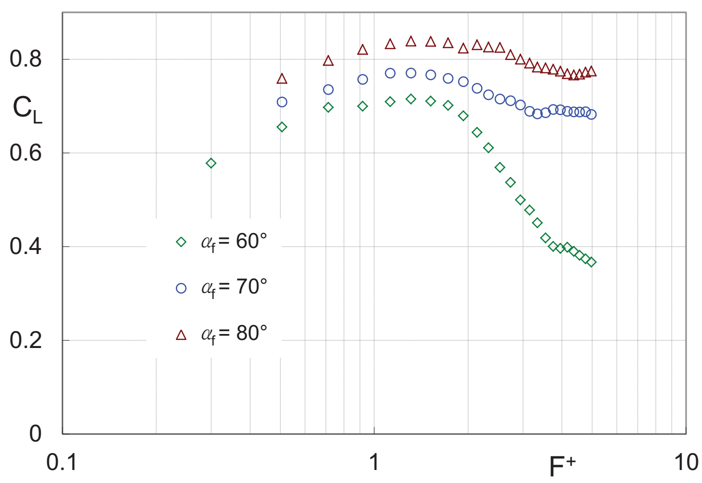

Figure 8. Example of lateral-force coefficient data as a function of reduced frequency for different DBD plasma forcing angles (Re = 80,000; C_μ = 0.17%, DC = 10%); from [7].

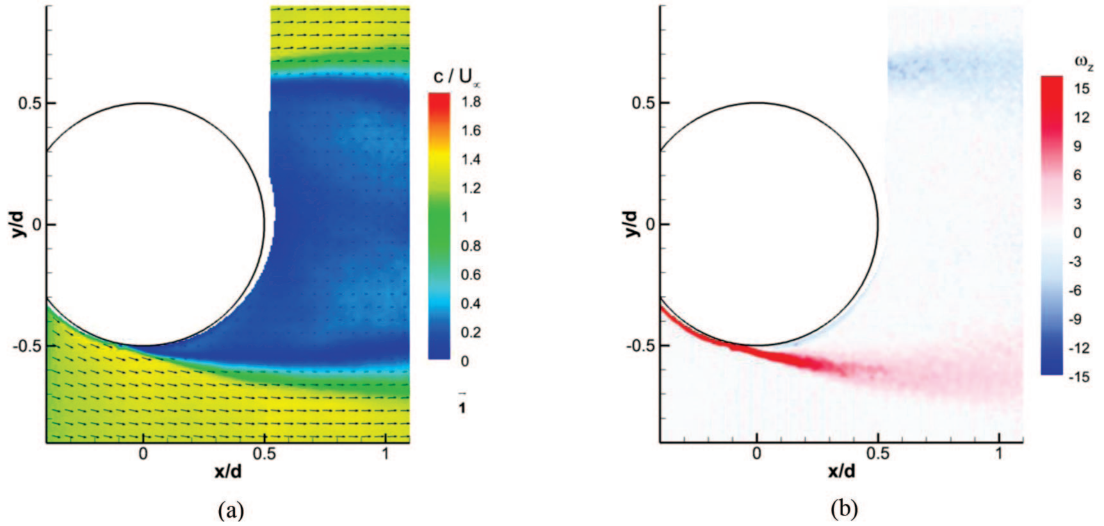

Figure 9. PIV flowfield measurements at the cylinder center-span for the baseline case at Re = 80,000: (a) absolute velocity $c = (u^2 + v^2)^{1/2}$; (b) spanwise vorticity ω_z.

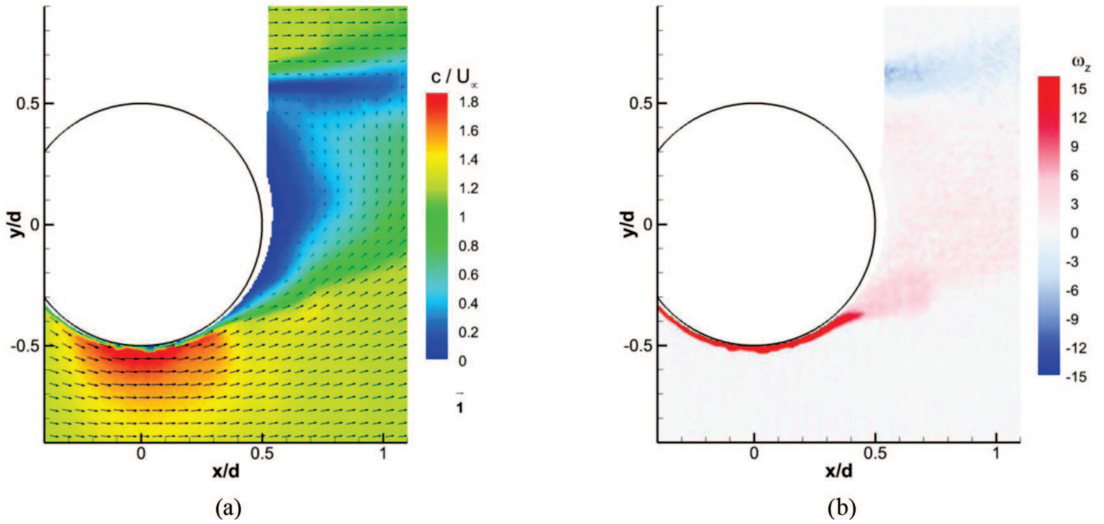

Figure 10. PIV flowfield measurements at the cylinder center-span for the $F^+ = 2.1$, DC = 10%, C = 0.17% case at Re = 80,000: (a) absolute velocity $c = (u^2 + v^2)^{1/2}$; (b) spanwise vorticity ω_z.

surface over approximately seven pulsations, or over the dimensionless time $\tau_{att} \equiv T_{att}U_\infty/d \approx 7/F^+$, namely $\tau_{att} \approx 3.3$ at $F^+ = 2.1$. On the other hand, following termination, the separation process slower with $\tau_{sep} \equiv T_{sep}U_\infty/d > 18/F^+$ or $\tau_{sep} > 8.6$. The sum of these time-scales (≈ 12) were well within the anticipated half-cycle time-scales $\frac{1}{2}T_{ex}U_\infty/d \approx \frac{1}{2}U_\infty/f_m d \approx 34$. The attachment and separation time-scales T_{att} and T_{sep} were used in the numerical model described in section 7.

5. SYSTEM CALIBRATION

The present experiments were performed with the load attached for the purpose of estimating the damping coefficients by means of direct calibration. This facilitated subsequent computation of the average cycle power. Due to uncertainty associated with repeatability of the valve setting, all calibrations were performed with a fixed valve setting. The different damping coefficients were then achieved by varying the height of the damper above the pivot, namely by varying the lever length l' (as described in section 3). The damper was maintained in a horizontal orientation when the system was at rest (pendulum at $\theta = 0$) by varying both its height on frame as well as the rectangular section rod mounted on the upper part of the system above the pendulum. All calibrations were performed with zero wind speed in the tunnel ($U_\infty = 0$). For each calibration experiment, the pendulum was raised to its maximum angle and released. Data from the four damper pressure ports for a typical calibration are plotted in fig. 11. It can be seen that the unsteady readings from all ports are virtually identical and similar observations were made during power measurements discussed below. For all calibration and power measurements, the data from the four ports was averaged. For each lever length l' ten repetitions were performed and the results were averaged to get the final damping coefficient.

Combining the data from figs. 12 and 13, namely, $|F_d|$ versus $\dot{\theta}$, produced the data that were used to calibrate the damper. The calibration coefficients were determined by means of least squares curve fitting. Fig. 14 shows that square relationship expressed theoretically in equation 25 is well represented in the experiments.

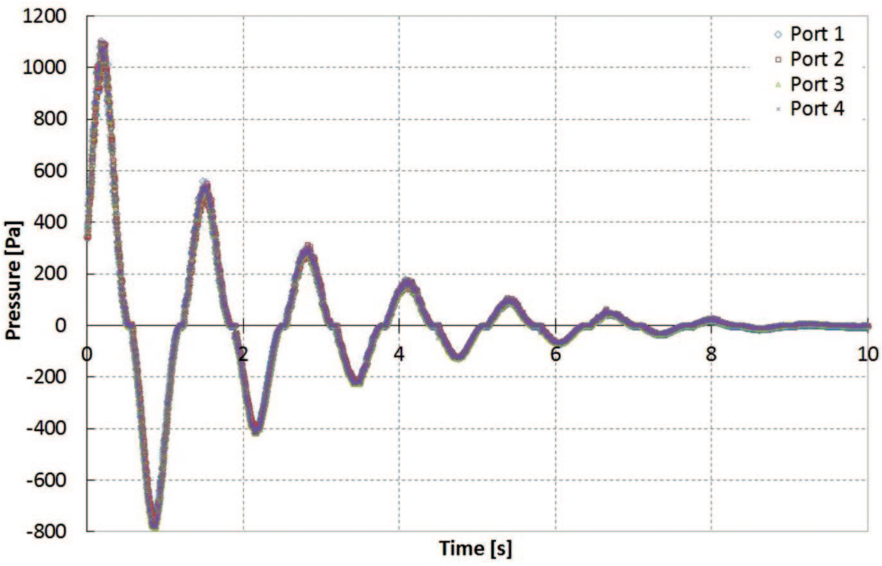

Figure 11. Data extracted from pressure ports shown in fig. 7.

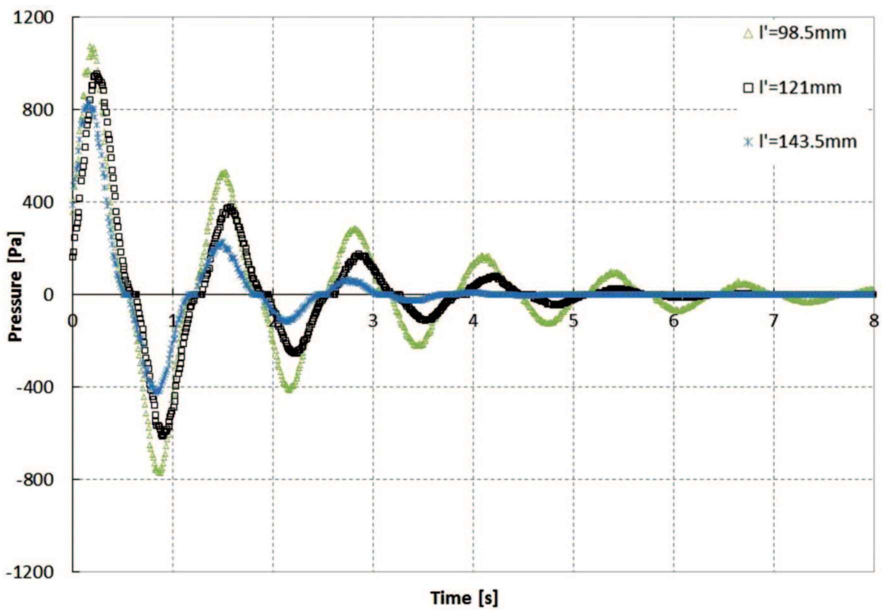

Figure 12. Pressure calibration data for different damper heights.

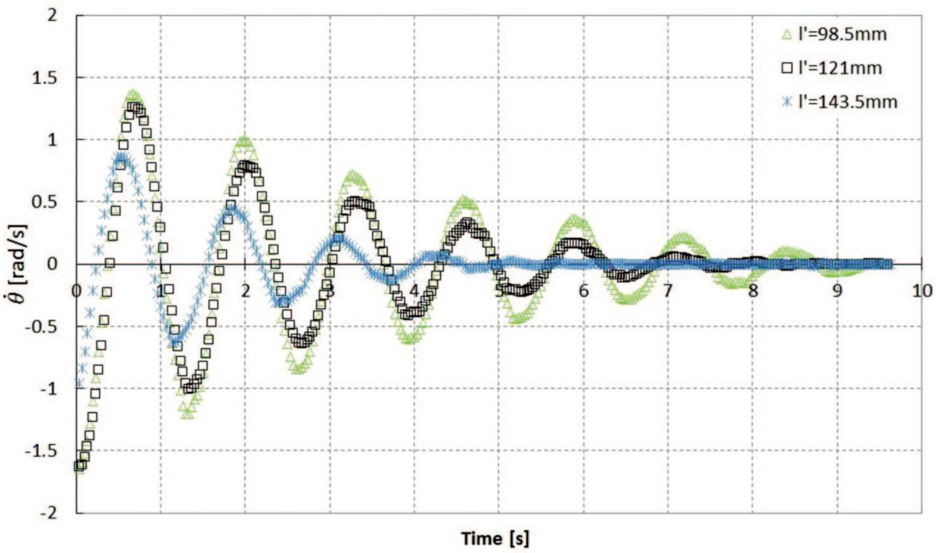

Figure 13. Angular velocity calibration data for different damper heights.

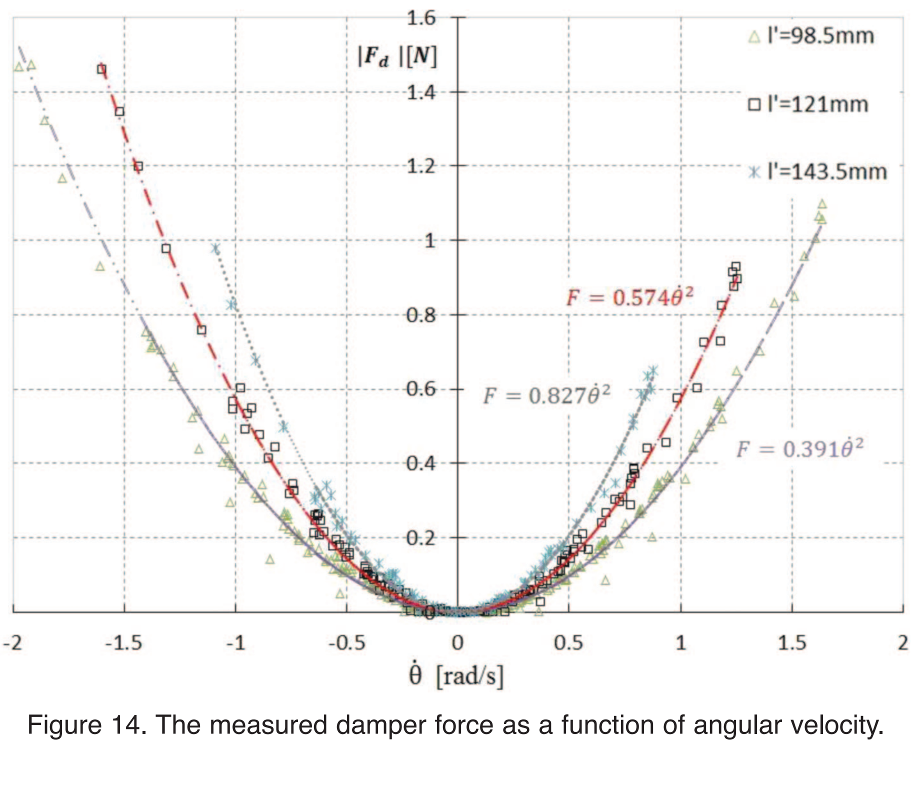

Figure 14. The measured damper force as a function of angular velocity.

When referring the force data to $\dot{x}$, as opposed to $\dot{\theta}$, the damping should theoretically remain constant namely, independent of the lever length l'. To check this, the experimental data in fig. 14 were plotted in fig. 15 as $|F_d|$ versus $\dot{x}$ and clearly show that for all lever lengths, the data points collapse onto the same line. This representation clearly illustrates the fidelity of the calibration.

Frictional losses in the pivot bearing were negligible but this was not the case for friction in the damper, where the frictional torque was calcuated according to:

$$M_f = l'(\mu m_p g + q_\infty C_L S \sin\theta) \tag{28}$$

where μ is the friction coefficient (0.2 based on the manufacturers specification), m_p is the measured mass of the pivoted piston.

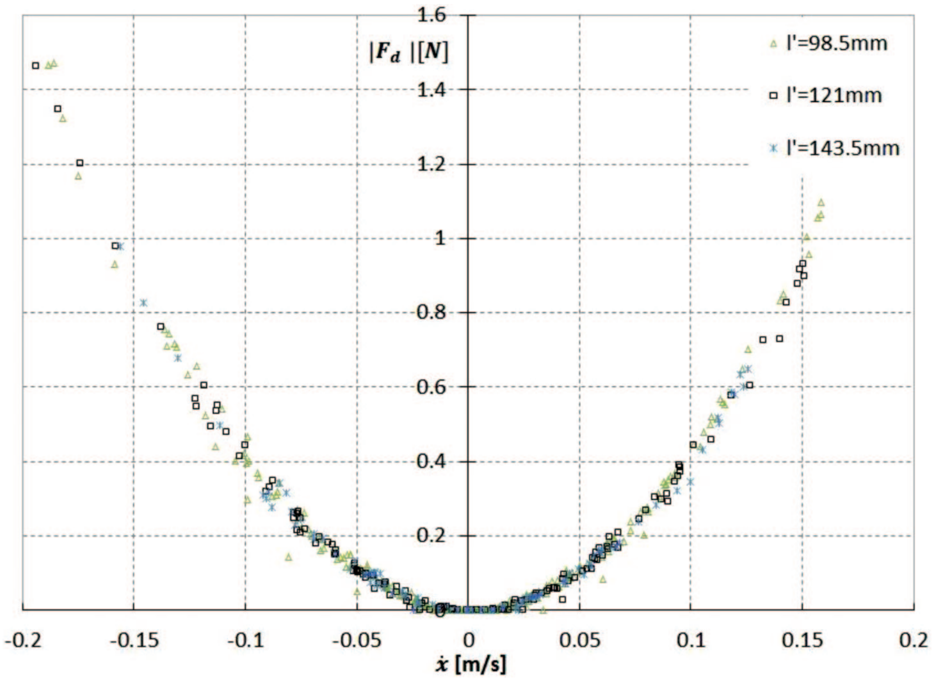

Figure 15. The measured damper force as a function linear velocity.

6. POWER CALCULATION

To produce nominally symmetric forcing the two plasma actuators were located at $\alpha = \pm 80°$ because these produced the largest lateral force coefficients for the present setup. The two optical sensors were located on the base plate above the wind tunnel ceiling and were configured to trigger each of the actuators independently. The sensors were deployed symmetrically and the angle at which they were triggered ($\pm\theta_{on}$) could be varied arbitrarily. The system could be configured in several ways. The plasma could be activated immediately upon receiving the signal from the sensor, or it could be configured with a delay before activating. The plasma's actuation time T_{act} operation time could also be varied arbitrarily by varying the number of plasma pulses. For each damper height several combinations of plasma initiation, activation time, and delay after plasma activation were selected. The camera and the ESP modules were triggered simultaneously. Sufficient time was given to the transient phenomena to decay. Experiments were repeated until the maximum integrated power was achieved. For each combination of parameters, experiments were performed initially using 10% duty cycle. Once the maximum power produced by the system was obtained then the duty cycle was systematically reduced in order to produce the maximum net system power. In some instances, only a small effect on the performance was observed for duty cycles as low as 1%.

As mentioned above, pressure and $\dot{\theta}$ were measured simultaneously. Pressure was measured using the ESP modules and $\dot{\theta}$ was calculated based on the pendulum's position data captured by the camera. The force operating on the damper (F_d) was then calculated from the pressure data. Figure 16 shows $\dot{\theta}$ and F_d on the same axis for a typical experiment and small cycle-to-cycle variations were observed. In order to obtain a statistically representative average, all power results were based on the average of forty cycles.

The average power developed over one cycle was calculated according to:

$$P = \frac{1}{T}\int_0^T F_d(t)\dot{x}(t)dt \tag{31}$$

Substituting $F_d(t) = p_d(t)A_p$ and $\dot{x}(t) = l'\dot{\theta}$, we can estimate the average power developed over N cycles as:

$$P = \frac{A_p l'}{NT}\int_0^{NT} p_d(t)\dot{\theta}(t)\,dt \tag{32}$$

where here $N = 40$.

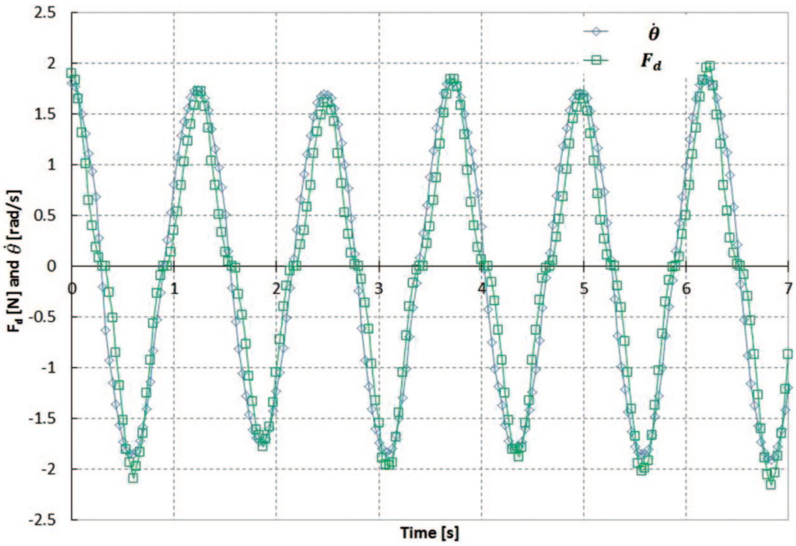

Figure 16. Simultaneous representation of the damper force and angular velocity for l' = 121 mm.

7. MODEL VALIDATION

Free decay calculations were performed by means of a fourth-order Runge-Kutta method and validated by comparing the results with experimental data at U_∞ = 8 m/s. An example comparison with the damper connected at l' = 98.5 mm is shown in fig. 17. The graphs shows a comparison of experimental data with a linear model employing arbitrarily chosen damping, as well as the measured calibrated quadratic damping with and without the effect of damper friction. The analytic model shows that an equivalent overall linear damping coefficient can be selected (or calibrated) that adequately represents the combined effect of the quadratic load and constant friction. Similarly, a linear load damping can also be selected where friction is separately taken into account. A comparison of the two quadratic damping cases clearly shows the impact of friction on the results. Shortly after releasing the cylinder, where the damper forces are large relative to friction, the differences between the peaks is relatively small. However, as the amplitude decreases, the frictional and load forces become comparable.

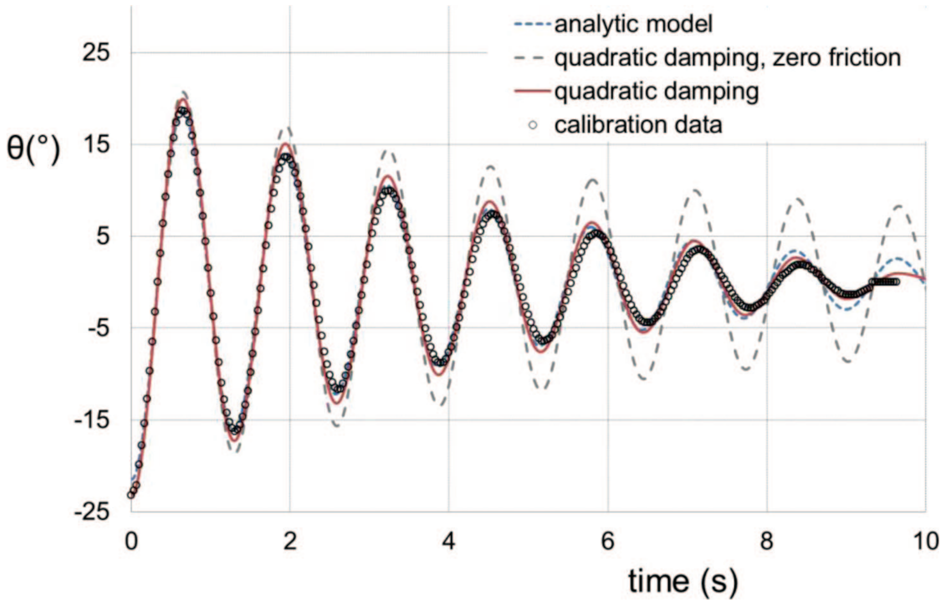

Figure 17. Model prediction of free decay under the influence of an arbitrary linear damping and the calibrated quadratic damping with and without the effect of friction (Coulomb damping).

This clearly shows that neglecting friction has a significant adverse effect on the predictions. Indeed, between 10 and 25 seconds the predicted amplitude without friction decreases by only one-half.

Forcing calculations were performed by solving equations 21 (linear damping) and 27 (quadratic damping) by means of a fourth-order Runge-Kutta method. The driving moment $M(t)$ was generated by means of a piecewise linear model: ramp-up to constant lift; constant lift maintained; and ramp-down to zero for each half-cycle. The ramp-up and ramp-down time-scales were T_{att} and T_{sep} as described in section 4 and the maximum lateral force coefficient estimated by the method shown in fig. 8 (see [7] for further details). When one actuator was installed on the cylinder, as in [7], a maximum value C_L = 0.83 was achieved; however, with both actuators installed the maximum was 0.65. This difference was traced to the addition of the second actuator that had the presumed effect of partial passive tripping the boundary layer and thus rendering the plasma pulses on the opposite side less effective. An example of cylinder displacement as a function of time for l' = 98.5 mm and a free-stream velocity U_∞ = 8 m/s are shown in fig. 18. Damping coefficients for both the analytic model and the linear damping were chosen arbitrarily to provide the same displacement angles. In contrast, the effects of Coulomb damping were included in the quadratic damping calculations of equation (21). Although the quadratic damping computations slightly under-predict the experimental amplitudes, the overall correspondence is good. In addition, the expected overshoot exhibited by linear analytic model, as a consequence of the small-angle assumption, is clearly evident. Similar calculations were performed for l' = 121 mm and 143.5 mm and a summary of the results is shown in fig. 19. For the purposes of comparing linear and quadratic loads, an effective damping coefficient $\zeta_{\text{eff}} = c_q\dot{\theta}_{\text{rms}}/2J_0\omega_n$ was defined.

Here the correspondence between the experiments and quadratic damping prediction is excellent. Note that as the damping coefficient tends to zero, the oscillation amplitude increases significantly until it is only Coulomb damping that is limiting the motion. The unbounded increase in angle predicted by the analytical model is not valid because the small angle assumption is violated.

Simultaneously measurements of $p_d(t)$ and $\dot{\theta}(t)$ were used together with equation (32) to calculate the average power and power coefficients developed at U_∞ = 8 m/s for successively increasing quadratic damping: l' = 98.5 mm, 121 mm and 143.5 mm. These were compared with power coefficient predictions and are shown in fig. 20. For the computations, C_L and hence $M_0 = R \cdot F_0$ were estimated by means of direct measurement, similar to the data shown in fig. 8. Thus, when we account properly for the load and friction, the correspondence between the data and computations is excellent, apart from the largest damping coefficient corresponding to l' = 143.5 mm that shows a slight under-prediction of the measurement. Note that lower damping was not considered because it caused the cylinder to collide with the wind tunnel walls. Here the effect of friction and aerodynamic drag can clearly be seen by

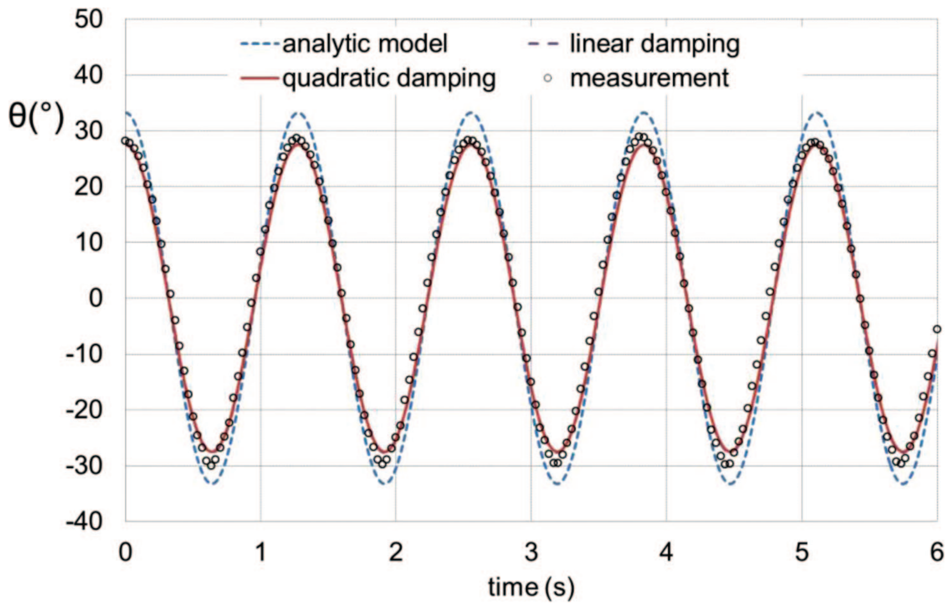

Figure 18. Displacement of the cylinder as a function of time under the effects of forcing at l'=98.5 mm, for U_∞ = 8 m/s; nominal *Re* = 80,000.

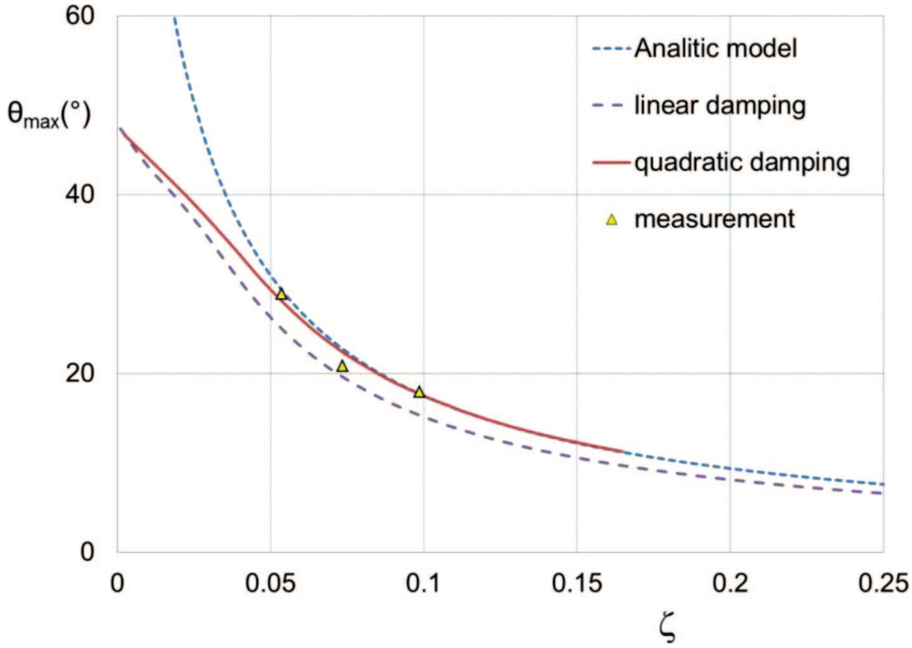

Figure 19. Maximum cylinder deflection angle predictions as a function of damping coefficient with experimental data at l' = 98.5 mm, 121 mm and 143.5 mm, for U_∞ = 8 m/s; nominal Re = 80,000.

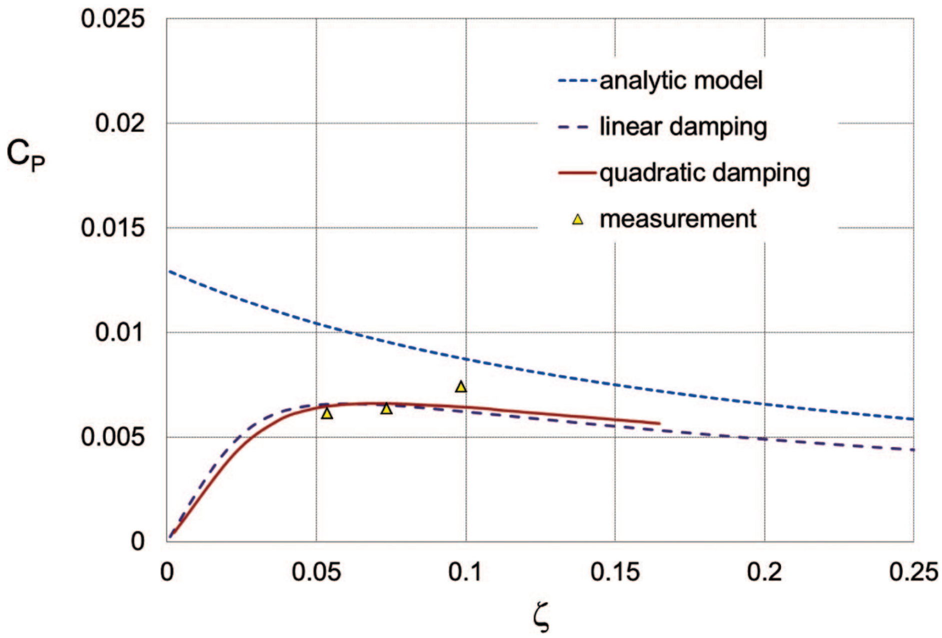

Figure 20. System power coefficient predictions together with experimental data as a function of damping coefficient with at l' = 98.5 mm, 121 mm and 143.5 mm, for U_∞ = 8 m/s; nominal Re = 80,000.

comparing the useful power quadratic predictions with the analytical ones. At low damping coefficients, the relative effect of friction is greater and hence there is a large disparity between the predictions. With increasing load the disparity becomes smaller. This effect is exacerbated at lower free-stream velocities. For example, at U_∞ = 4m/s where the dynamic pressure and hence forces are reduced by a factor of four, this disparity becomes even larger (fig. 21). In addition to the relatively large effects of friction, the theoretical value of C_P increases with decreasing U_∞ as seen from equation

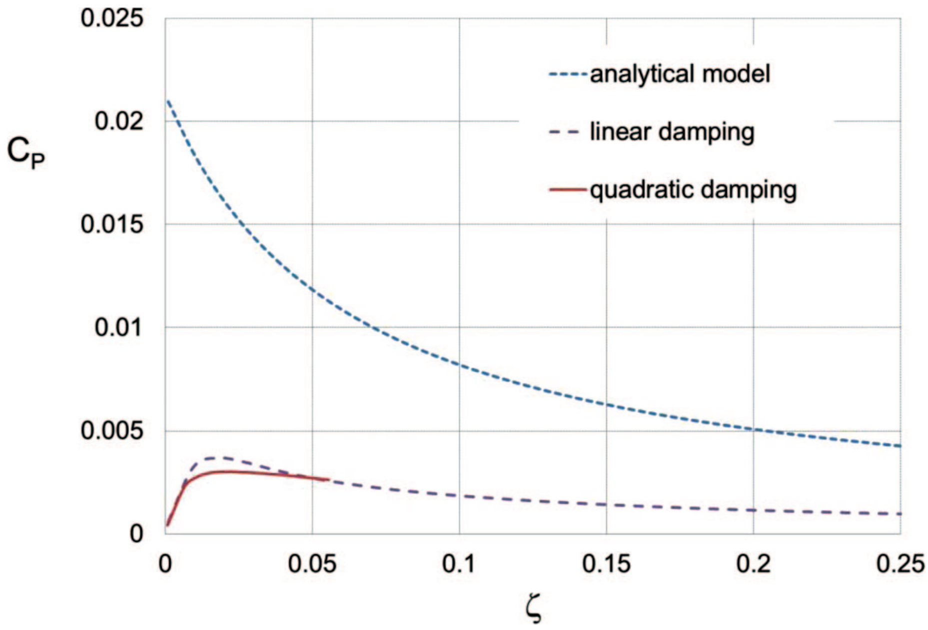

Figure 21. System power coefficient predictions as function of damping coefficient for $U_\infty = 4$ m/s.

20. This can clearly be seen by comparing figs. 20 and 21. In contrast, increasing the model free-stream velocity to $U_\infty = 12$ m/s, namely increasing the aerodynamic forces by more than two, reduces the disparity between the ideal and useful power (see fig. 22).

Systematic reductions to both T_{on} (or DC) as well as T_{act}, facilitated a significant reduction in the gross power supplied to the actuators. For the data presented in figs. 19 and 20, the gross power supplied to the actuators was 10 and 11 milliwatts respectively. This is because the actuator was driven at DC = 1% with T_{act}/T_{ex} = 20%. This should be compared with the maximum integrated power measured in the experiments, namely 210 milliwatts (see fig. 23) that is a factor of 10 larger than the total power input to the plasma actuators. Thus, although the power coefficient of the present system is low, less than 1% at 8m/s, the power produced is significantly larger than the power required to drive the actuators.

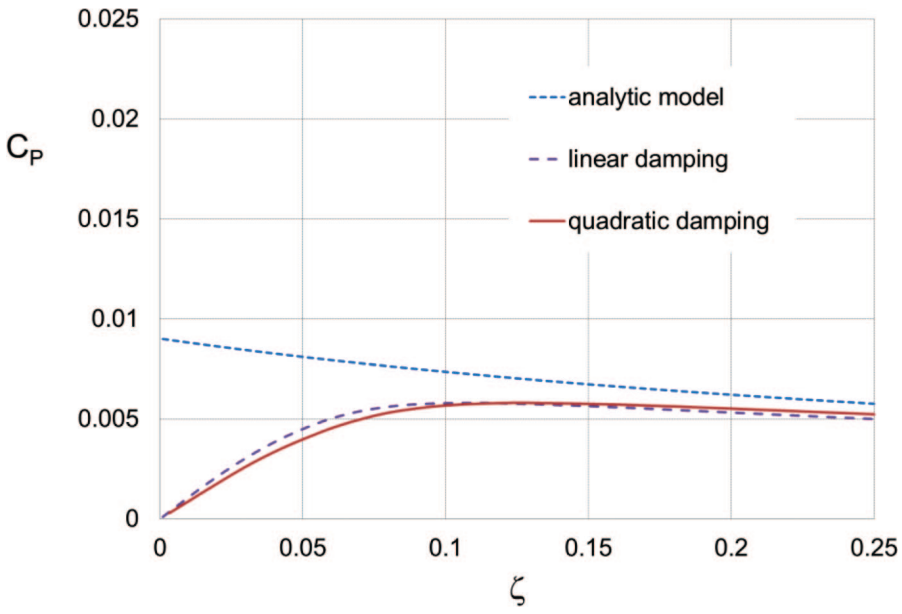

Figure 22. System power coefficient predictions as function of damping coefficient for $U_\infty = 12$ m/s; nominal Re = 120,000.

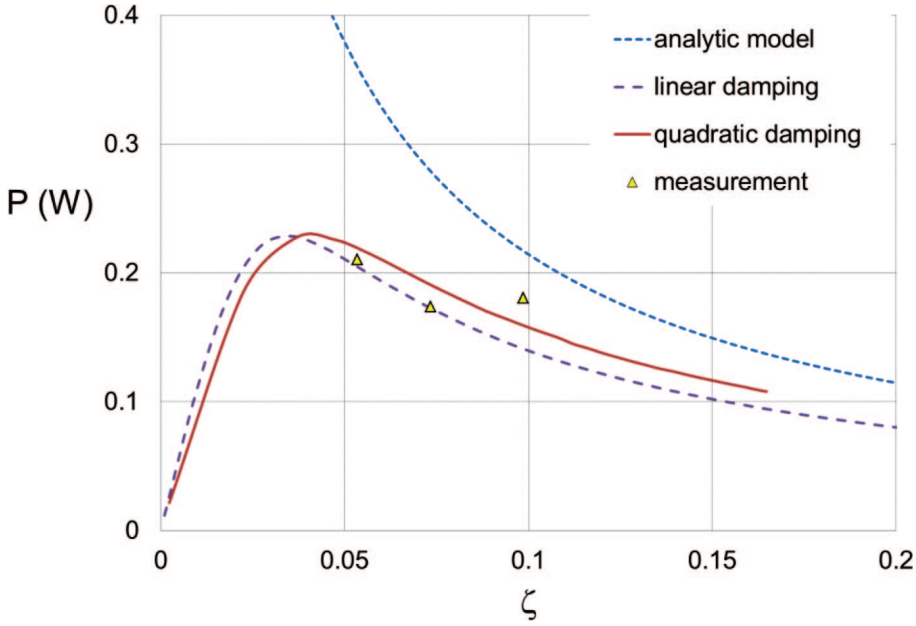

Figure 23. System power predictions as function of damping coefficient with experimental data at l' = 98.5 mm, 121 mm and 143.5 mm, for U_∞ = 8m/s; nominal Re = 80,000.

8. VIABILITY FOR WIND ENERGY GENERATION

Given the very low power coefficients produced by this system, it appears unlikely that a system based on the present design could credibly pose a challenge to conventional wind power generation via HAWTs. Moreover, the super-critical Reynolds numbers (>300,000) expected with larger dimensions cause the separation point to move downstream and reduce the control authority. Nevertheless, before ruling out larger-scale power generation, it is worth considering several methods that could conceivably be implemented to significantly increase efficiency and thereby render the concept viable.

Conceptually, a simple approach would be to add additional cylinders. In this way, the power produced by the system will theoretically be increased by the number of additional cylinders. Another conceptually simple method would be to increase the lateral force coefficient by actively changing the aerodynamic shape and/or using a more powerful actuation method. Equation 20 shows that for a 1-DOF system, the power coefficient is directly proportional to the lateral force coefficient. A survey of techniques [7] for lateral force generation on circular cylinders concluded that steady slot blowing ($C_l \approx 7.9$, with momentum coefficients $C_\mu \approx 0.56$) or porous suction ($C_l \approx 5.65$ with $C_Q \approx Q / dU_\infty = 0.2$ where Q is the air volumetric flowrate) could increase the power coefficient by an order of magnitude; the two techniques could also be used simultaneously. However, the power required to drive the blowing and suction systems, relative to the power gain, may be excessive and is a critical metric for determining their viability. One option available to reduce the power required is to use so-called fluidic actuators of the type studied by Gokoglu et al. [9].

Larger-scale power generation would obviously require up-scaling the system. If we consider a linear scaling such that the system dimensional ratios remain constant, it can be shown that the power coefficient increases with $R^{½}$ [7]. Unfortunately, a simple prediction of power increases cannot easily be made because increasing the size significantly increases the cylinder velocity normal to the wind direction. This violates our assumption $R\dot{\theta}_{max} << U_\infty$. In such a case, the aerodynamic efficiency of the cylinder and the cylinder velocity relative to the wind velocity will be decisive parameters in determining the system power.

It was also noted in [7] that flow control over a cylinder result in changes to the drag coefficient. These variations may then be exploited by adding a second degree-of-freedom (2-DOF) to the system, as mentioned in section 1, by allowing the system to oscillate in the streamwise direction. In this manner, the controlled periodic drag oscillations could also be exploited to extract power from the system. The mathematical model of such a system would require the consideration of the fully non-linear two degree-of-freedom equations. Although the development of such a model is beyond the scope of this paper, it should be considered as an important component of future research.

9. CONCLUDING REMARKS

To the best knowledge of the authors, this paper presented the first active-flow-control-induced vibration wind-energy generator. The vibrations were achieved by means of two symmetrically mounted DBD plasma actuators that were employed to force alternate attachment and separation of the boundary layer, thereby producing the forces to drive the system close to resonance. A nonlinear load, typical of a positive displacement fluid pump, was attached to the system and instrumented with pressure transducers. Under phase-locked actuation, simultaneous pressure and angular displacement measurements were performed to determine the integrated mean system power.

A system model, including non-linear load effects, aerodynamic effects and friction was developed. Peak measured power coefficients were relatively small, less than 1% and predictions of were excellent. Friction was found to play a significant role in reducing the power output of the generator. Nevertheless, the power input to the actuators required to drive the system, was a factor of 10 lower that the integrated power produced.

The power coefficients were very small when compared to conventional wind turbines, namely less than 1%. Nevertheless, this was merely a demonstration study and several techniques could be used to increase this, such as changing the shape of the aerodynamic body, increasing the number of cylinders, utilizing blowing or suction to maximum lateral force coefficients, increasing the system natural frequency or increasing the cylinder diameter. Priorities for future research should incorporate a 2-DOF mathematical model, more effective forms of boundary layer control and system dimensional scaling.

NOMENCLATURE

A_p	piston area
A_j	jet exit area
c_d	damping coefficient due to aerodynamic drag
c_l	linear load damping coefficient
c_q	quadratic lkoad damping coefficient
C_l	two-dimensional lateral-force coefficient
C_L	maximum cylinder lateral-force coefficient, $F_0/½\ \rho U_\infty^2 dh$
C_P	power coefficient, $P/q_\infty U_\infty A_s$
C_θ	the angular damping coefficient
d	cylinder diameter
DC	duty cycle
f	system oscillation frequency
f_{ex}	structural excitation frequency, $1/T_{\mathrm{ex}}$
f_{ion}	plasma ionization frequency
f_n	pendulum natural frequency, $1/T_n$
f_p	plasma pulsing frequency, $1/T_p$
F_0	maximum cylinder lateral-force
F^+	dimensionless plasma pulsing frequency, $f_p d/U_\infty$
F_p	force applied to the piston
h	cylinder height, $R_0 - R_i$.
J_0	system moment of inertia with respect to the pivot
k_t	“dynamic stiffness”, $mgl_{CG.}$
l'	distance from pivot to rigid connecting rod
l_{CG}	distance from the pivot to the center of mass
m	total mass of the system
$M(t)$	driving moment
M_0	moment maximum
p_{atm}	atmospheric pressure
p_p	pressure applied to the piston
P	gross power produced

P_p plasma input power
q_∞ free-stream dynamic pressure, $1/2\rho U_\infty^2$
R distance from the pivot to the center of the cylinder
R_i distance from the pivot to inner edge of the cylinder
R_o distance from the pivot to outer edge of the cylinder
Re nominal Reynolds numbers, $U_\infty d/v$
t time
T_{act} time of pulsed plasma actuation
T_{att} time-scale associated with forced flow attachment
T_{ex} structural excitation period
T_{sep} time-scale associated with forced flow separation
U_∞ free-stream velocity
V voltage
V_{pp} peak-to-peak voltage
x free-stream direction
y cross-stream direction
α cylinder angle from the plane parallel to U_∞
ϕ phase-angle
θ system deflection angle
τ dimensionless time, TU_∞/d
ω circular oscillation frequency, $2\pi f$
ω_n circular natural frequency, $2\pi f_n$
ζ linear damping coefficient, $c_l/2J_0\omega_n$
ζ_{eff} effective damping coefficient for a non-linear load, $c_q\dot{\theta}_{\text{ms}}/2J_0\omega_n$

REFERENCES

[1] Anon., "World Wind Energy Report 2010," World Wind Energy Association. February 2011. ww.wwindea.org/home/images/stories/pdfs/worldwindenergyreport2010_s.pdf. Retrieved 26 September, 2011.

[2] Barlas, T.K. and van Kuik, G.A.M., 2010. Review of state of the art in smart rotor control research for wind turbines. Progress in Aerospace Sciences 46, 1–27.

[3] Bade, P., 1976. Flapping-vane wind machine. Proceedings of the International Conference of Appropriate Technologies for Semiarid Areas: Wind and Solar Energy for Water Supply, 83–88.

[4] Jeffery, J.R., 1977. Oscillating aerofoil project. Report from the Pocklington School Design Centre, West Green, Pocklington, York, England.

[5] McKinney, W., and DeLaurier, J., 1981. The wingmill: An oscillating-wing windmill. AIAA Journal of Energy 5 (2), 109–115.

[6] Bernitsas, M.M., Raghavan, K., Ben-Simon, Y., and Garcia, E.M.H., 2008. VIVACE (Vortex induced vibration aquatic clean energy): A new concept in generation of clean and renewable energy from fluid flow, Journal of Offshore Mechanics and Arctic Engineering 130.

[7] Greenblatt, D., Treizer, A., Eidelman, A. and Mueller-Vahl, H., 2012. Flow-Control-Induced Vibrations using Pulsed DBD Plasma Actuators. Journal of Fluids & Structures, 34, 170–189.

[8] Corke, T.C., Post, M.L., and Orlov, D.M., 2007. SDBD plasma enhanced aerodynamics: Concepts, optimization and applications. Progress in Aerospace Sciences 43, 193–217.

[9] Gokoglu, S.A., Kuczmarski, M.A., Culley, D.E. and Raghu, S., "Numerical Studies of a Fluidic Diverter for Flow Control," AIAA Paper No. 2009-4012, 39th AIAA Fluid Dynamics Conference, 22–25 June 2009, San Antonio, Texas.

[10] Greenblatt, D. and Wygnanski, I., 2000 "The control of separation by periodic excitation," *Progress in Aerospace Sciences*, Volume 36, Issue 7, pp. 487–545.

[11] Thomas, F.O., Kozlov, A. and Corke, T.C., 2008 "Plasma Actuators for Cylinder Flow Control and Noise Reduction," AIAA Journal Vol. 46, No. 8, pp. 1921–1931.

[12] Jukes, T.N. and Choi, K.-S., 2009 "Control of unsteady flow separation over a circular cylinder using dielectric-barrier-discharge surface plasma," Physics of Fluids, Vol. 21, 094106.